EXACT SOLUTION FOR MULTISPECTRAL AND HYPERSPECTRAL FUSION VIA HESSIAN INVERSION

Dan Pineau, François Orieux, Alain Abergel

Université Paris-Saclay, CNRS, CentraleSupélec, Laboratoire des Signaux et Systèmes, France
Université Paris-Saclay, CNRS, Institut d'Astrophysique Spatiale, France

ABSTRACT

Multispectral and hyperspectral data fusion allows the restoration of data with increased spatial and spectral resolutions. A common approach is to solve an ill-posed inverse problem by minimizing a regularized least squares criterion. This minimization usually requires an iterative gradient-based method, but this paper demonstrates the existence of an explicit solution. Direct models of the imager and the spectrometer are described, the explicit solution is developed, and an application on simulated data from the James Webb Space Telescope is presented. A potential time saving of a factor of 1 000 is highlighted by the proposed method.

Index Terms— inverse problems, hyperspectral, data fusion, astronomical data, JWST

1. INTRODUCTION

Many fields such as remote sensing, astrophysics or Earth observation use hyperspectral data for spectra observation. Several applications allow the use of integral field spectrographs to acquire spectra in a given field of view, but the images produced are generally poorly sampled. Parallel acquisition of high spatial resolution and well sampled data, such as multispectral data, opens the field of data fusion to reconstruct highly spatially and spectrally resolved data [1].

Approaches for data fusion are often based on the solution of inverse problems with the minimization of a criterion including a data adequacy term [2]. This method requires both knowledge of the data formation process, called forward model, and a model of the observed object.

In Wei *et al.* (2015) [3], the MS/HS data fusion problem is formulated through a Sylvester equation, and an explicit solution to this inverse problem is obtained, allowing a significant reduction of the computational cost unlike iterative approaches. However, this method is not applicable to the reconstruction of astronomical data because it is developed without spatial blur variability. Guilloteau *et al.* (2020) [4] proposes the solution of an inverse problem adapted to astronomical data with a spectrally non-stationary spatial blur by minimizing a least squares criterion with quadratic regularization. But unlike Wei *et al.*, an iterative algorithm is then pro-

posed to approximate the solution. The approach proposed here computes the exact solution in an explicit way without requiring an iterative optimization algorithm.

The instrument models are presented in section 2, and the problem and its explicit solution are presented in section 3. Section 4 presents an application of our method on simulated astronomical data acquired by instruments similar to MIRI of the James Webb Space Telescope (JWST). The results are presented in terms of reconstruction quality and time saving compared to an iterative method.

2. MODELS DESCRIPTION

2.1. Observed object model

The observed sky region is described as a discrete hyperspectral cube $\boldsymbol{x}$ with two spatial coordinates $i \in [1, I]$ and $j \in [1, J]$, and a spectral coordinate $l \in [1, L]$. As proposed in [5, 4, 6], spectral correlations are introduced within the observed object $\boldsymbol{x}$, such that the spectral content of any location (i, j) is a linear combination of T known spectra $\boldsymbol{s}_t$. The observed object $\boldsymbol{x}$ thus writes as

$$\boldsymbol{x}[i,j,l] = \sum_{t=1}^{T} \boldsymbol{a}_t[i,j] \, \boldsymbol{s}_t[l] \tag{1}$$

where $\boldsymbol{a}_t[i, j]$ gives the abundance of the spectrum $\boldsymbol{s}_t$ at (i, j). This assumption, known as the Linear Mixing Model, offers several advantages: as the spectra $\boldsymbol{s}_t$ are defined for all common wavelengths covered by the instruments, they enable efficient joint processing of all available data. In addition, this model reduces the number of unknowns describing the observed object from $I \times J \times L$ to $I \times J \times T$, with $T \ll L$, reducing the computational load. Equation 1 can be rewritten in a matrix form as

$$\boldsymbol{x} = \boldsymbol{T}\boldsymbol{a} \tag{2}$$

where $\boldsymbol{T}$ is the linear mixing matrix, written as

$$\boldsymbol{T} = \begin{pmatrix} \boldsymbol{s}_1[1]\boldsymbol{I}_P & \dots & \boldsymbol{s}_T[1]\boldsymbol{I}_P \\ \vdots & & \vdots \\ \boldsymbol{s}_1[L]\boldsymbol{I}_P & \dots & \boldsymbol{s}_T[L]\boldsymbol{I}_P \end{pmatrix} \tag{3}$$

and I_P is the identity matrix of size $P \times P$, with $P = I \times J$ the number of pixels in an image.

2.2. Imager model

This model takes into account several types of transformations on the observed object:

1. a spectrally varying spatial blur due to the instrument's impulse response h_{m},

2. the spectral response w_{m}, dependent on mirrors and imager filters characteristics and detector quantum efficiency,

3. the spectral integration performed for each of the C imager filters.

The data produced by the imager from the object x are C images, produced with a spatial sampling step equal to that of x. Therefore, the value of a pixel at position (i, j) in image $c \in [1, C]$ is written as

$$x_{\mathrm{m}}^c[i,j] = \sum_l (x \underset{i,j}{*} h_{\mathrm{m}})[i,j,l]\, w_{\mathrm{m}}^c[l] \qquad (4)$$

where $\underset{i,j}{*}$ is the spatial convolution operator. This equation writes in a matrix form as

$$x_{\mathrm{m}} = W_{\mathrm{m}} C_{\mathrm{m}} x \qquad (5)$$

where C_{m} is a block diagonal matrix, whose diagonal contains L circulant convolution matrices $C_{\mathrm{m},l}$ operating the spatial blur h_{m} for each wavelength of x, and the matrix W_{m} operates the spectral response and spectral integration. Integrating the Linear Mixing Model of equation 2 into this equation leads to

$$x_{\mathrm{m}} = W_{\mathrm{m}} C_{\mathrm{m}} T a \qquad (6)$$

where $M = W_{\mathrm{m}} C_{\mathrm{m}} T$ is the identified matrix form imager model, made up of $C \times T$ blocks. Thus a block of M at the row c and column t is expressed as

$$M_{c,t} = \sum_l w_{\mathrm{m}}^c[l] s_t[l] C_{\mathrm{m},l}. \qquad (7)$$

2.3. Spectrometer model

The transformations induced by the spectrometer model contain

1. a spectrally varying spatial blur due to the impulse response h_{h} of the instrument,

2. the spectral response w_{h}, linked to the mirrors characteristics, the diffraction grating and the detector response,

3. integration and spatial sampling of the detector, which can be insufficient and lead to spectral aliasing.

The data produced by the spectrometer from the object x are then L images with a spatial sampling step d_i times greater in height and d_j times greater in width than the one used in x, with $d_i, d_j \in \mathbb{N}^*$. Pixels are therefore located in a new reference frame with coordinates $(\bar{i}, \bar{j})$, and their value writes as

$$x_{\mathrm{h}}[\bar{i}, \bar{j}, l] = \sum_{i=\bar{i}d_i}^{(\bar{i}+1)d_i} \sum_{j=\bar{j}d_j}^{(\bar{j}+1)d_j} (x \underset{i,j}{*} h)[i,j,l]\, w_{\mathrm{h}}[l] \qquad (8)$$

which, as for the imager model, possesses a matrix form with the integrated linear mixing matrix T that writes

$$x_{\mathrm{h}} = \overline{S} W_{\mathrm{h}} C_{\mathrm{h}} T a \qquad (9)$$

where C_{h} has the same structure as C_{m}, i.e. with L matrices $C_{\mathrm{h},l}$ on its diagonal to operate the spatial blur h_{h}, W_{h} operates the spectral response at L wavelengths, and $\overline{S} = I_L \otimes S$ is a matrix operating the integration and sampling of the detector by a convolution operation with a kernel of size $d_i \times d_j$ filled with "1", and a selection of 1 pixel over d_i pixels in height and d_j pixels in width. The matrix form of the spectrometer model is identified as $H = \overline{S} W_{\mathrm{h}} C_{\mathrm{h}} T$, built with $L \times T$ blocks, and the block at the row l and column t is expressed as

$$H_{l,t} = w_{\mathrm{h}}[l] s_t[l] S C_{\mathrm{h},l}. \qquad (10)$$

3. METHODOLOGY

This section proposes a formulation of the inverse problem to be solved for the reconstruction of the observed object, and then describes an explicit solution to the problem posed.

3.1. Formulation of the problem

The abundance maps $\hat{a}$ describing the observed object are defined as the minimizer of a quadratic criterion $\mathcal{J}$, as proposed in Guilloteau *et al.* [4], composed of two data adequacy terms and a regularization term as

$$\hat{a} = \underset{a}{\operatorname{argmin}} \{\mathcal{J}(a)\}$$
$$= \underset{a}{\operatorname{argmin}} \{\mu_{\mathrm{m}}\|y_{\mathrm{m}} - Ma\|_2^2 + \mu_{\mathrm{h}}\|y_{\mathrm{h}} - Ha\|_2^2 + \mu_{\mathrm{r}}\|\overline{D}a\|_2^2\}$$
$$(11)$$

where $\mu_{\mathrm{m}} = \frac{1}{2\sigma_{\mathrm{m}}^2}$, $\mu_{\mathrm{h}} = \frac{1}{2\sigma_{\mathrm{h}}^2}$, and σ_{m} and σ_{h} are the standard deviations of additive white gaussian noises assumed to be present in the imager data y_{m} and spectrometer data y_{h}, respectively. The regularization parameter $\mu_{\mathrm{r}} \in \mathbb{R}_+$ regulates the influence of the spatial smoothness imposed to stabilize the solution, and $\overline{D} = I_T \otimes D$ where D is a first order 2D

difference matrix. The minimization of $\mathcal{J}$ is performed by solving $\nabla \mathcal{J} = 0$, giving

$$\hat{a} = Q^{-1} b \qquad (12)$$

with

$$Q = \mu_{\mathrm{m}} M^H M + \mu_{\mathrm{h}} H^H H + \mu_{\mathrm{r}} \overline{D}^H \overline{D} \text{ , and} \qquad (13)$$

$$b = \mu_{\mathrm{m}} M^H y_{\mathrm{m}} + \mu_{\mathrm{h}} H^H y_{\mathrm{h}} \text{ ,} \qquad (14)$$

where $\cdot^H$ is the conjugate transpose operator. Therefore, the minimizer $\hat{a}$ of the quadratic criterion $\mathcal{J}$ can be calculated explicitly if the inversion of the hessian Q is possible without being a computational burden. Its inversion is explained in the next section.

3.2. Explicit solution

The three matrices $M^H M$, $H^H H$ and $\overline{D}^H \overline{D}$ consist of $T \times T$ blocks. An explicit expression for the block at the row t and column t' of each of these matrices is

$$(M^H M)_{t,t'} = \sum_c M_{c,t}^H M_{c,t'} \qquad (15)$$

$$(H^H H)_{t,t'} = \sum_l w_{\mathrm{h}}[l]^2 s_t[l] s_{t'}[l] C_{\mathrm{h},l}^H S^H S C_{\mathrm{h},l} \qquad (16)$$

$$(\overline{D}^H \overline{D})_{t,t'} = D^H D \qquad (17)$$

with $M_{c,t}$ described equation 7. Since the blocks of these matrices are circulant, they are diagonalizable in Fourier space. Indeed,

1. $(M^H M)_{t,t'}$ is written as products and weighted sums between circulant convolution matrices $C_{\mathrm{m},l}$, so each block is also circulant,

2. $(H^H H)_{t,t'}$ is also circulant, as $C_{\mathrm{h},l}^H S^H S C_{\mathrm{h},l}$ writes in the Fourier space

$$C_{\mathrm{h},l}^H S^H S C_{\mathrm{h},l} = F^H \Lambda_l^H F S^H S F^H \Lambda_l F \qquad (18)$$

with F the Fourier matrix, and Λ_l the diagonal matrix of the eigenvalues of $C_{\mathrm{h},l}$. However, since S corresponds to a spatial decimation and S^H to a filling of "0", $S^H S$ has as its diagonal a Dirac comb with a "1" every $d_i d_j$ coefficients. Thus $F S^H S F^H$ is a circulant convolution matrix, as presented in Wei *et al.* (2015) [3], such that

$$F S^H S F^H = \frac{1}{d_i d_j} J_{d_i d_j} \otimes I_{P'} \qquad (19)$$

with $\otimes$ standing for the Kronecker product, $J_{d_i d_j}$ is a square matrix of size $d_i d_j \times d_i d_j$ and full of 1, and $P' = \frac{P}{d_i d_j}$ is the number of pixels in an image after applying S. Therefore, $C_{\mathrm{h},l}^H S^H S C_{\mathrm{h},l}$ is a matrix of diagonal blocks in Fourier space, and so are the blocks of $H^H H$.
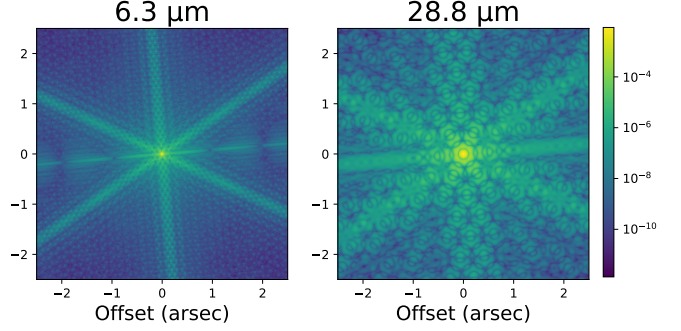
Fig. 1: MIRI PSF [7] (logarithmic scale).

3. $D^H D$ is also circulant by approximating D as a circulant matrix.

Consequently, according to equation 13, the $T \times T$ blocks of Q are also diagonalizable in Fourier space. An expression for Q is then

$$Q = \overline{F}^H B_Q \overline{F} \qquad (20)$$

where B_Q is a matrix of diagonal blocks, and $\overline{F} = I_T \otimes F$. Inverting B_Q is possible by transforming this matrix into a block-diagonal matrix Δ_Q with a permutation matrix P, such that

$$B_Q = P \Delta_Q P. \qquad (21)$$

According to equations 20 and 21, the inversion of Q is calculated as follows

$$Q^{-1} = \left(\overline{F}^H P \Delta_Q P \overline{F} \right)^{-1} \qquad (22)$$

$$= \overline{F}^H P^T \Delta_Q^{-1} P^T \overline{F} \qquad (23)$$

where $\cdot^T$ is the matrix transpose operator, and Δ_Q^{-1} is computable by inverting each of its blocks individually. The data are then reconstructed explicitly with the equation 12, as proposed in [5], thus avoiding the use of an iterative optimization method [4].

4. EXPERIMENTAL RESULTS

One targeted application of this work concerns the fusion of imaging and spectrometry data from the mid-infrared instrument MIRI of the JWST. The instrument models described in parts 2.2 and 2.3 have been adapted to the imager MIRIM [8] and Medium Resolution Spectrometer (MRS) [9] of MIRI.

The impulse response h used here is simulated by *webbpsf* [7], and figure 1 illustrates its spectral dependency. The imager contains $C = 9$ filters and its spectral response is taken into account with the real Photon Conversion Efficiency (PCE) curves of MIRIM [10]. The spectrometer model considered here uses decimation factors $d_i = d_j = 4$ (summing
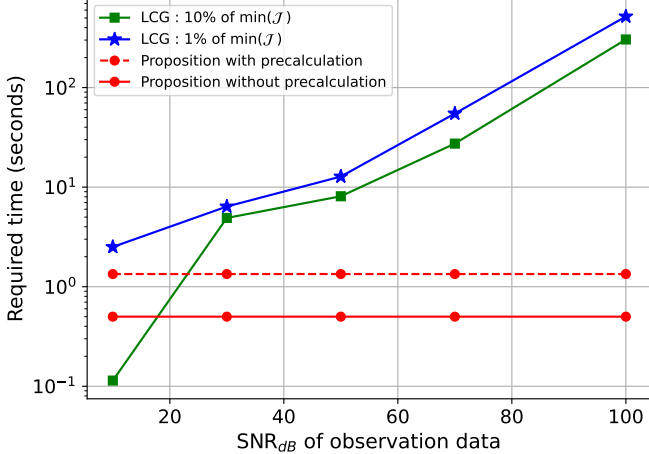
Fig. 2: Time required by the LCG algorithm to reach 10% and 1% of the minimum of the criterion $\min(\mathcal{J})$ (equation 11), compared with the time required by the proposed explicit solution as a function of the SNR_{dB} of the instrument data. Calculations with i9-10885H processor, 2.40 GHz (x 16), RAM 64 GB.

the values of each 4×4 pixel region into 1), inducing spectral aliasing of the received signal for wavelengths below 20 µm. The MRS has 4 spectral channels with 3 sub-channels each, leading to 12 different PCE curves [9]. However, the spectrometer considered here is simplified with a single channel and a PCE curve produced by concatenating the PCE curves of the MRS [10].

Imagery data $\boldsymbol{y}_{\text{m}}$ and spectrometry data $\boldsymbol{y}_{\text{h}}$ data have been created by applying the imager and spectrometer models on a set $\boldsymbol{a}$ of $T = 5$ spectral abundance maps [11, 12], associated to their respective spectrum $\boldsymbol{s}_t$ [13], to describe the observed object using the Linear Mixing Model of equation 1. These maps were simulated from real observational data from the Orion Bar, and contain 125×250 pixels. The spectra cover the MIRI band (5 to 28 µm), and contain $L = 300$ values. These observation data $\boldsymbol{y}_{\text{m}}$ and $\boldsymbol{y}_{\text{h}}$ were corrupted with an additive white gaussian noise of standard deviations σ_{m} and σ_{h}, respectively.

Figure 3 illustrates the quality of the spatial reconstruction of the observed object for two different noise cases: a case of low noise where the signal to noise ratio SNR_{dB} is 50 dB for both the imagery data $\boldsymbol{y}_{\text{m}}$ and the spectrometry data $\boldsymbol{y}_{\text{h}}$ (see figure 3a), and a case of high noise where $\text{SNR}_{\text{dB}} = 20$ dB for both sets of data (see figure 3b). Reconstruction errors are evaluated using the Normalized Root Mean Square Error (NRMSE) [14], given under each figure, where NRMSE $= \|\hat{\boldsymbol{x}} - \boldsymbol{x}\|_2 \, / \, \|\boldsymbol{x}\|_2$, where $\boldsymbol{x}$ is the original hyperspectral cube describing the object, and $\hat{\boldsymbol{x}}$ is the estimated cube. The first case demonstrates an effective deconvolution effect, as spatial features are successfully deblurred compared to the instrument data. The second case illustrates the algorithm resilience

to gaussian noise as most spatial features, which disappeared in the instrument data, are recovered. Moreover, the average error between the spectra observed by the spectrometer and the original spectra can exceed 30 mJy arcsec^{-2} for both noise cases, whereas the average error with the reconstructed spectra does not exceed 1 mJy arcsec^{-2}.

Furthermore, tests were carried out to compare the iterative approach [4] and the proposed explicit approach in terms of the computation time required to solve the equation 11. The two approaches were tested by choosing the value of μ_{r} that minimizes the NRMSE with respect to the original data. The iterative approach LCG (Linear Conjugate Gradient) requires a computation time exponentially proportional to the SNR_{dB} of the data $\boldsymbol{y}_{\text{m}}$ and $\boldsymbol{y}_{\text{h}}$, as shown figure 2. For a very low noise case ($\text{SNR}_{\text{dB}} = 100$ dB), more than 8 minutes are needed with LCG to reach 1% of $\min(\mathcal{J})$. Indeed, the less noisy the data, i.e. the higher the SNR_{dB}, the less spatial regularization is required for optimal reconstruction, and the more high frequencies need to be restored, requiring a greater number of iterations. This problem is avoided with the proposed explicit solution, as the time needed to reach $\min(\mathcal{J})$ is constant: 1.34 seconds with precalculations (creation and inversion of the hessian $\boldsymbol{Q}$), but only 0.5 seconds without precalculations (single calculation of $\hat{\boldsymbol{a}} = \boldsymbol{Q}^{-1}\boldsymbol{b}$).

5. CONCLUSION

The imager and spectrometer models were described by considering spectrally varying blurs, instrument spectral responses, imager spectral integrations, and spectrometer spatial integrations and subsampling. The data fusion problem was posed by formulating a least-squares quadratic criterion to be minimized. The existence of an explicit solution has been demonstrated.

The results showed not only improved spatial and spectral resolutions, deconvolution and noise reduction, but also considerable time savings compared to an iterative approach: a factor of 1 000 for a low noise case ($\text{SNR}_{\text{dB}} = 100$ dB) without precalculations (factor greater than 300 when precalculations are taken into account), for the reconstruction of 5 abundance maps of size 125×250, and thus of a cube of size $125 \times 250 \times 300$ thanks to a linear mixing model.

Edge-preserving techniques, such as the use of semi-quadratic or convex regularization, would improve the quality of the reconstructed cubes. Studies will be carried out to verify the existence of an explicit solution for such methods.

6. REFERENCES

[1] Naoto Yokoya et al., "Hyperspectral and multispectral data fusion: A comparative review of the recent literature," *IEEE Geoscience and Remote Sensing Magazine*, vol. 5, no. 2, pp. 29–56, 2017.

(a) SNR$_{\text{dB}}$ of instruments data : 50 dB, NRMSE = 0.0103.

(b) SNR$_{\text{dB}}$ of instruments data : 20 dB, NRMSE = 0.0226.
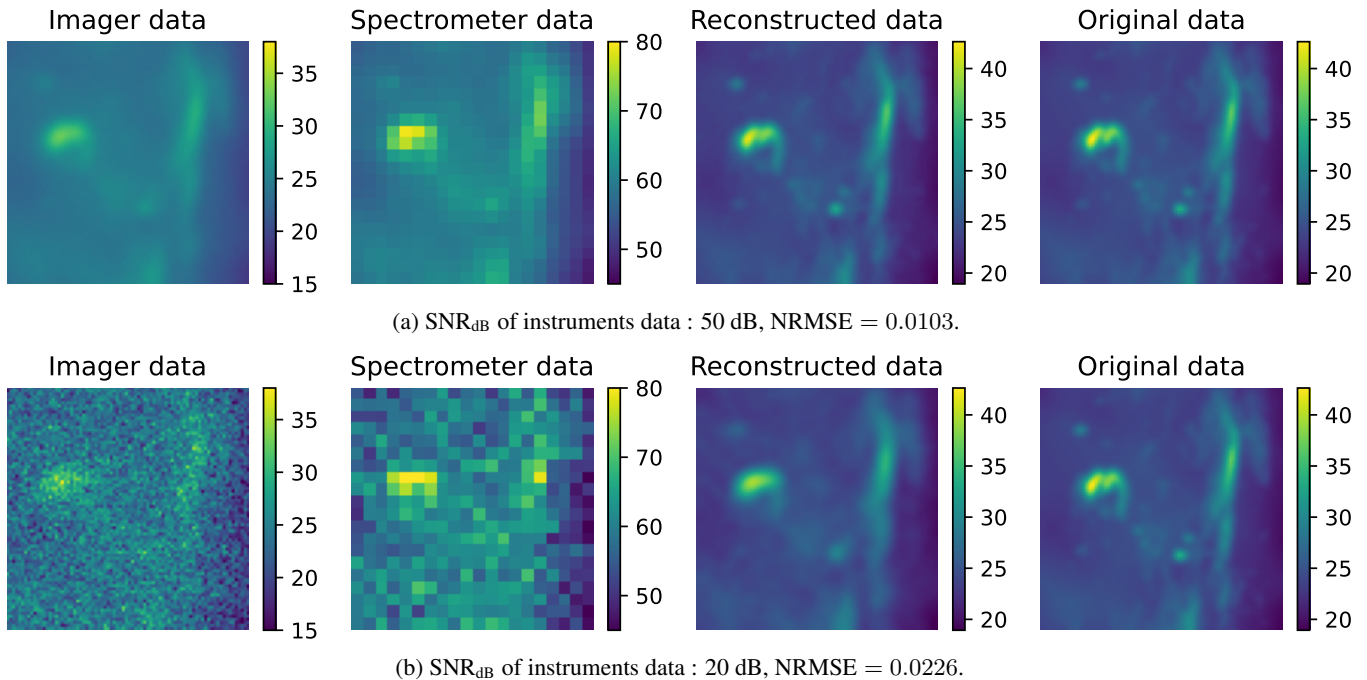
Fig. 3: Imagery data y_{m} at the sixth spectral band, spectrometry data y_{h}, reconstructed data $\hat{x}$, and original data x. SNR$_{\text{dB}} =$ 50 dB for the instrument data for figure 3a, and SNR$_{\text{dB}} = 20$ dB for figure 3b. All images are those observed (or centered for the imager) at 15.5 μm. Unit in mJy arcsec^{-2}.

[2] Jérôme Idier et al., "Approche bayésienne pour les problèmes inverses," *Hermès, Paris*, vol. 3, 2001.

[3] Qi Wei et al., "Fast fusion of multi-band images based on solving a sylvester equation," *IEEE Transactions on Image Processing*, vol. 24, no. 11, pp. 4109–4121, 2015.

[4] Claire Guilloteau et al., "Hyperspectral and multispectral image fusion under spectrally varying spatial blurs–application to high dimensional infrared astronomical imaging," *IEEE Transactions on Computational Imaging*, vol. 6, pp. 1362–1374, 2020.

[5] Mohamed Elamine Hadj-Youcef, *Spatio spectral reconstruction from low resolution multispectral data: application to the Mid-Infrared instrument of the James Webb Space Telescope*, Ph.D. thesis, Université Paris-Saclay (ComUE), 2018.

[6] Ralph Abi-Rizk et al., "Super-resolution hyperspectral reconstruction with majorization-minimization algorithm and low-rank approximation," *IEEE Transactions on Computational Imaging*, vol. 8, pp. 260–272, 2022.

[7] Marshall D Perrin et al., "Simulating point spread functions for the james webb space telescope with webbpsf," in *Space Telescopes and Instrumentation 2012: Optical, Infrared, and Millimeter Wave*. SPIE, 2012, vol. 8442, pp. 1193–1203.

[8] Patrice Bouchet et al., "The mid-infrared instrument for the james webb space telescope, iii: Mirim, the miri imager," *Publications of the Astronomical Society of the Pacific*, vol. 127, no. 953, pp. 612, 2015.

[9] Martyn Wells et al., "The mid-infrared instrument for the james webb space telescope, vi: The medium resolution spectrometer," *Publications of the Astronomical Society of the Pacific*, vol. 127, no. 953, pp. 646, 2015.

[10] STScI, "JWST documentation website," https://jwst-sdocs.stsci.edu, Accessed: 2023-03-06.

[11] Claire Guilloteau et al., "Simulated jwst data sets for multispectral and hyperspectral image fusion," *The Astronomical Journal*, vol. 160, no. 1, pp. 28, 2020.

[12] Emilie Habart et al., "High angular resolution near-ir view of the orion bar revealed by keck/nirc2," *arXiv preprint arXiv:2206.08245*, 2022.

[13] PI Team, Olivier Berné, et al., "Pdrs4all: A jwst early release science program on radiative feedback from massive stars," *Publications of the Astronomical Society of the Pacific*, vol. 134, no. 1035, pp. 054301, 2022.

[14] J. R. Fienup, "Invariant error metrics for image reconstruction," *Appl. Opt.*, vol. 36, no. 32, pp. 8352–8357, Nov 1997.